SIMULATIONS OF AUTONOMOUS FLUID PULSES BETWEEN ACTIVE ELASTIC WALLS USING THE 1D-IRBFN METHOD

Fatima Z. Ahmed[1,3], Mayada G. Mohammed[2], Dmitry V. Strunin[1,*]
and Duc Ngo-Cong[1]

Abstract. We present numerical solutions of the semi-empirical model of self-propagating fluid pulses (auto-pulses) through the channel simulating an artificial artery. The key mechanism behind the model is the active motion of the walls in line with the earlier model of Roberts. Our model is autonomous, nonlinear and is based on the partial differential equation describing the displacement of the wall in time and along the channel. A theoretical plane configuration is adopted for the walls at rest. For solving the equation we used the One-dimensional Integrated Radial Basis Function Network (1D-IRBFN) method. We demonstrated that different initial conditions always lead to the settling of pulse trains where an individual pulse has certain speed and amplitude controlled by the governing equation. A variety of pulse solutions is obtained using homogeneous and periodic boundary conditions. The dynamics of one, two, and three pulses per period are explored. The fluid mass flux due to the pulses is calculated.

1. Introduction

The present paper is focused on a mathematical model to simulate an *artificial* artery with *actively* moving walls. Putting aside the technological challenges of construction of such a sophisticated device, we aim to establish theoretical principles of how the artificial walls need to move in order to facilitate a uni-directional fluid flow. This is the main purpose of this work, in distinction to the models of real biological vessels [2, 4, 7, 15]. Note that the recent years saw a remarkable progress in design and fabrication of artificial muscles. For example, the recent paper [9] describes the fluid-driven and origami-inspired artificial muscles which can be programed to achieve not only contraction, but also bending and torsion at multiple scales.

Our analysis is based on the model [16], which further develops the ideas of Roberts of channels with active walls [14]. While Roberts considered the case of negligible viscous forces compared to inertia, which is relevant to wider channels, we will consider the case when inertia is negligible compared to viscous forces, which is relevant to narrow channels.

---

[1] Faculty of Health, Engineering and Sciences, University of Southern Queensland, Toowoomba, QLD 4350, Australia.
[2] Department of Mathematics, University of Thi-Qar, Nasiriyah, Iraq.
[3] Department of Mathematics, University of Kirkuk, Kirkuk, Iraq.

* Corresponding author: strunin@usq.edu.au

Roberts considered a long cylindrical channel with cross-sectional area $A(x,t)$. With the x-axis directed along the channel, the mass continuity equation is written as

$$\frac{\partial A}{\partial t} + \frac{\partial (Av)}{\partial x} = 0\,,$$

where $v(t)$ is the velocity of the fluid flow. Substituting the circular cross section, $A = \pi R^2$, where $R(x,t)$ is the radius of the channel, we get

$$\frac{\partial R}{\partial t} + v\frac{\partial R}{\partial x} + \frac{1}{2}R\frac{\partial v}{\partial x} = 0\,. \tag{1.1}$$

Because the wall's material is elastic, an increase in the local pressure leads to an increase in the radius,

$$p - p_* = \alpha(R - R_*)\,, \tag{1.2}$$

where p_* and R_* are the neutral pressure and radius of the channel respectively and $\alpha > 0$ is a constant which depends on mechanical characteristics of the wall. The momentum equation without viscous friction has the form

$$\frac{\partial v}{\partial t} + v\frac{\partial v}{\partial x} = -\frac{1}{\rho}\frac{\partial p}{\partial x}\,, \tag{1.3}$$

where ρ is the fluid density. Substituting (1.2) into (1.3), we get

$$\frac{\partial v}{\partial t} + v\frac{\partial v}{\partial x} = -\frac{\alpha}{\rho}\frac{\partial R}{\partial x}\,, \tag{1.4}$$

Equations (1.1) and (1.4) form a system of two equations with respect to the two unknown functions $R(x,t)$ and $v(x,t)$. Assuming that they experience only small departures, $\hat{R}$ (from R_*), and $\hat{v}$ (from 0), using (1.1)–(1.3) we obtain the wave equation

$$\frac{\partial^2 \hat{v}}{\partial t^2} = c_*^2 \frac{\partial^2 \hat{v}}{\partial x^2}\,,$$

where $c_* = [\alpha R_*/(2\rho)]^{1/2}$. Its D'Alembert's solution

$$\hat{v} = f(x - c_* t) + g(x + c_* t)$$

describes waves travelling in an unchanging form with the speed c_*.

Roberts postulated that the wall, when it contracts, produces an extra pressure term in the p–R relationship,

$$p = p_* + \alpha(R - R_*) + P(x,t)\,, \tag{1.5}$$

where $P(x,t)$ is the prescribed function of x and t. Substituting (1.5) into the continuity and momentum equations (1.1), (1.3) and linearizing we get the forced linear wave equation

$$\frac{\partial^2 \hat{v}}{\partial t^2} = c_*^2 \frac{\partial^2 \hat{v}}{\partial x^2} - \frac{1}{\rho}\frac{\partial^2 P}{\partial x \partial t}\,, \tag{1.6}$$

where the last term is responsible for the active action of the wall. The active pressure is assumed to have the form of a wave,

$$P(x,t) = P_0(t - x/c_0),$$

where P_0 has the shape of a twitch (pulse). It describes a squeezing motion which travels down the artery with the speed c_0. The general solution of equation (1.6) is

$$\hat{v} = \frac{c_0}{\rho(c_0^2 - c_*^2)} P_0(t - x/c_0) + f(x - c_*t) + f(x + c_*t),\tag{1.7}$$

which describes the forced flow due to the action of the wall and also the free, elastic wave propagating along the channel. Observe the difference $c_0^2 - c_*^2$ in the denominator in (1.7). Roberts pointed out that, if the speed of the forced wave is sufficiently close to the speed of the free elastic wave, the forced wave becomes very large. We add that this is a resonant-type phenomenon where the external force is synchronized with the self-oscillation of the system. Loosely the dynamic is as follows. The force kick-starts a wave which propagates to the neighbouring region with the speed c_*. Simultaneously the force itself, represented by P_0, moves to that region and kicks again (of course, this is not a discrete but a smooth process). Since the speed of the force, c_0, is close to c_*, the force is effectively synchronized with the pulse. The product of $c_0/(c_0^2 - c_*^2) \cdot P_0$ represents a non-decaying pulse caused by the active motion of the wall.

The fact that P_0 explicitly depends on t and x suggests that the resulting pulse-shaped solution (1.7) is dictated by the force and has a prescribed shape (Roberts suggested that P_0 should be linked to the action of the heart). From mathematical viewpoint, this renders the model non-autonomous.

Strunin [16] formulated an autonomous model of pulse propagation. For simplicity he considered a theoretical configuration of the flow contained between unbounded active elastic walls shaped (in the rest state) as planes. The model was partly derived from physical principles, namely the classical lubrication theory for the flow coupled with the theory of elasticity for the wall, and partly using phenomenological arguments.

In line with the Roberts model, Strunin assumed that synchronization takes place, however in a different form to [14]. He supposed that the walls help the pulse to propagate by exerting extra pressure and extra shear stress at any location along the channel at the time when the pulse arrives at that location. But unlike the model [14] he considered the case when viscous friction dominates over inertia. This is done via the lubrication theory based on the balance between the pressure gradient and viscous friction. The phenomenology of the model transpires through specific form of additional terms representing active components of the pressure and shear stress produced by the walls. Using the dynamical system terminology, our model can be classified as active-dissipative and the pulses as auto-waves, that is self-supported dissipative structures. Unlike conservative waves, for example surface waves in fluids, the auto-waves have unique values of the velocity, width and amplitude.

The model had to meet the following requirements: (1) it should yield pulse-shaped auto-wave solutions; (2) these solutions should be "basic" that is an arbitrary initial condition would always break down into more or less identical pulses, their shape and speed being determined by the system's dynamical laws and not the initial conditions; (3) the motion of the wall should be cyclic, that is every small piece of the wall should return to its initial position after each pulse; this would ensure that the wall remains undisplaced on average; (4) the pulses propagate in one direction only; (5) the pulses transport fluid mass in that direction; and (6) the model should include viscous effects. The model [16] satisfies requirements (1)–(6); it has the form (2.17) presented in the next section.

In the short preliminary paper [1], we demonstrated some examples of pulse-type solutions of equation (2.17) in its integrated form (written with respect to the function f such that $\partial f/\partial x = w$). In the current paper, we analyze the original w-equation (2.17) and present a wide range of pulse regimes. We continue the paper by presenting the derivation of the model in Section 2 enhanced by the introduction of the eigenvalue K necessary to guarantee zero average displacement of the wall. The numerical method is described in Section 3.

In Section 4, we present the single-pulse solutions; in Section 5, we calculate the mass flux; and in Section 6, analyze multiple-pulse solutions. Conclusions are given in Section 7.

2. The autonomous viscous model

In this section we present derivation of the model, yet with an important modification relative to [16]. The modification ensures the natural requirement of zero average horizontal displacement of the wall. In the end of the section, we also present another new result, namely the final form of the model for cylindrical geometry.

We start with the flow between infinite elastic walls, assuming symmetry with respect to the middle plane, $z = 0$; hence, it will suffice to analyze only half of the flow, $1 < z < H(x, t)$ (Fig. 1). All unknown functions are uniform in the y-direction. Assuming that fluid inertia is small compared to viscous friction, we apply the lubrication theory [6], which equates the pressure gradient to the viscous force,

$$\frac{\partial^2 v}{\partial z^2} = \frac{1}{\eta} \frac{\partial p}{\partial x},\tag{2.1}$$

where x and z are the coordinates along and across the flow, respectively, $v(x, z, t)$ the flow velocity in the x-direction, $p(x, t)$ the pressure, and η is the viscosity. The pressure is assumed z-independent, so that integrating (2.1) on z gives

$$v = \frac{1}{2\eta} \frac{\partial p}{\partial x} \left(z^2 - H^2\right) + v(x, H, t).\tag{2.2}$$

The mass flux is

$$Q = \int_0^H v \, dz = -\frac{H^3}{3\eta} \frac{\partial p}{\partial x} + v(x, H, t) H.\tag{2.3}$$

We define the displacement, $w(x, t)$, of the wall in the z-direction from the neutral position, $H = H_0$, by

$$H = H_0 + w.\tag{2.4}$$

Then the continuity equation becomes

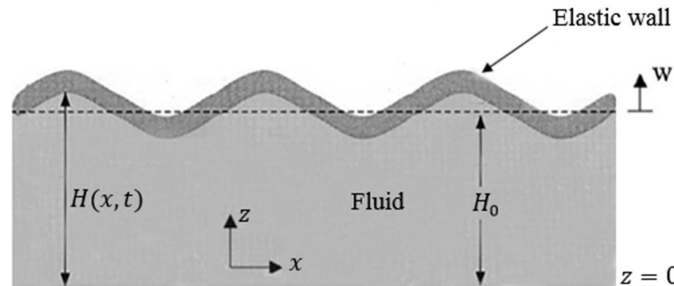$$\frac{\partial w}{\partial t} + \frac{\partial Q}{\partial x} = 0.\tag{2.5}$$

FIGURE 1. The fluid flow between elastic walls (half of the channel is shown).

Substituting (2.3) into (2.5) gives

$$\frac{\partial w}{\partial t} = \frac{\partial}{\partial x} \left[\frac{H^3}{3\eta} \frac{\partial p}{\partial x} - v(x, H, t) \, H \right] . \tag{2.6}$$

Equation (2.6) links the displacement of the flow boundary, coinciding with the wall's position, to the flow pressure. The elasticity theory [8, 20] provides the reverse link from the pressure to the displacement,

$$p = D \frac{\partial^4 w}{\partial x^4} - \frac{\partial}{\partial x} \left(N \frac{\partial w}{\partial x} \right) , \tag{2.7}$$

where

$$N = \frac{Eh}{1 - \nu^2} \left[\frac{\partial u}{\partial x} + \frac{1}{2} \left(\frac{\partial w}{\partial x} \right)^2 \right] . \tag{2.8}$$

In (2.7) and (2.8) $u(x, t)$ is the wall's displacement along the flow, D the flexural rigidity of the wall, E the Young's modulus, h the thickness of the wall, ν the Poisson's ratio, and N is the force caused by the displacements. Substituting (2.8) and (2.7) into (2.6), and using the no-slip boundary condition,

$$v(x, H, t) = \frac{\partial u}{\partial t} ,$$

we obtain

$$\frac{\partial w}{\partial t} = \frac{D}{3\eta} \left(H^3 w^V \right)' - \frac{Eh}{6\eta(1 - \nu^2)} \left[H^3 \left(w'^{\,3} \right)'' \right]'$$

$$- \frac{Eh}{3\eta(1 - \nu^2)} \left[H^3 (u'w')'' \right]' - \left(\frac{\partial u}{\partial t} H \right)' . \tag{2.9}$$

The shear stress in the fluid is represented as usual by $T = \eta \partial v / \partial z$, therefore on the boundary, $z = H$, using (2.2),

$$T = p' \, H . \tag{2.10}$$

This shear stress must be equal to the shear stress produced by the wall,

$$T = N' . \tag{2.11}$$

Equating (2.10) and (2.11) with the use of (2.8), we have

$$\frac{E}{1 - \nu^2} \left[u'' + \frac{1}{2} \left(w'^2 \right)' \right] = p' \, H . \tag{2.12}$$

The three equations (2.9), (2.12), and (2.7) form a closed system with respect to the three functions of interest, $w(x, t)$, $u(x, t)$, and $p(x, t)$. Now suppose that, when deflecting from the neutral position, the elastic walls exert

extra pressure relative to (2.7),

$$p = Dw^{IV} - (Nw')' + p_0 + p_1 \,, \tag{2.13}$$

where p_0 is the constant (reference pressure) and p_1 depends on w. We postulate that p_1 is proportional to the 4th power of the vertical displacement,

$$p_1 = -\alpha w^4 \,, \quad \alpha > 0 \,. \tag{2.14}$$

Further, we suppose that the walls actively move along the flow, thereby producing an extra shear stress relative to (2.12). We postulate that the wall's motion along the flow, represented by the displacement u and velocity $\partial u/\partial t$, is coupled with w. Specifically, the H-weighted velocity along the flow, $H\partial u/\partial t$, combined with the other u-containing term in (2.9), depends on w as

$$-\frac{Eh}{3\eta(1-\nu^2)}H^3(u'w')'' - \frac{\partial u}{\partial t}H = H^3\beta w^5 - K \,, \quad \beta > 0 \,, \tag{2.15}$$

where K is the constant. K is an eigenvalue of a settled pulse regime; it will be appropriately selected to ensure that the horizontal displacement of the wall after each pulse is zero. This relation implies that an extra (active) shear stress is applied by the wall; we denote it T_1. The total stress satisfies the continuity condition on the boundary

$$T_1 + \frac{E}{1-\nu^2}\left[u'' + \frac{1}{2}\left(w'^2\right)'\right] = p'H \,, \tag{2.16}$$

where the pressure p is represented by (2.13). Although we are not able to justify the concrete powers of w used in (2.14) and (2.15), these relations state that the larger the deformation w the larger the active response from the wall. Under the assumptions (2.13), (2.14), and (2.15), the equation (2.9) governing the dynamics of the vertical displacement becomes u-independent:

$$\frac{\partial w}{\partial t} = \frac{D}{3\eta}\left(H^3 w^V\right)' - \frac{Eh}{6\eta(1-\nu^2)}\left[H^3\left(w'^3\right)''\right]'$$

$$-\frac{1}{3\eta}\alpha\left[H^3\left(w^4\right)'\right]' + \beta\left(H^3 w^5\right)' \,. \tag{2.17}$$

It is important to require that the overall displacement of the wall over one period, T, is zero,

$$\int_T \frac{\partial u}{\partial t}\,\mathrm{d}t = 0 \,, \quad \int_T \frac{\partial w}{\partial t}\,\mathrm{d}t = 0 \,. \tag{2.18}$$

The second condition in (2.18) is guaranteed provided the boundary conditions are periodic. Indeed, each term in the equation's right-hand side (RHS) is a derivative and the expression under differentiation is periodic. The first condition of (2.18) can be transformed using (2.15) to the form

$$\int_T \left[-\frac{Eh}{3\eta(1-\nu^2)}H^2(u'w')'' - \beta H^2 w^5 + \frac{K}{H}\right]\,\mathrm{d}t = 0 \,, \tag{2.19}$$

which can be met by selecting K. The procedure of finding solution is as follows. The function $w(x,t)$ is obtained from (2.17) under periodic boundary conditions. Then $u(x,t)$ and K are found from (2.15), (2.19) for the settled

pulse regime. Lastly, the pressure is obtained from (2.13), (2.14), and the extra shear stress $T_1(x, t)$ and total stress from (2.16).

Qualitative analysis carried out in [16] shows that an individual pulse is the result of the dynamical balance between the three terms in the right side of equation (2.17). The term containing E is not crucial for the balance; it comes from the classical elasticity and has dissipative effect, while the crucial dissipative term is the 6th-order derivative. If E is sufficiently small, the E-containing terms can be neglected. In this case, the main equation (2.17) takes the simpler form

$$\frac{\partial w}{\partial t} = \frac{D}{3\eta} \left(H^3 w^V \right)' - \frac{1}{3\eta} \alpha \left[H^3 \left(w^4 \right)' \right]' + \beta \left(H^3 w^5 \right)' .$$
(2.20)

and the condition (2.19) becomes

$$\int_T \left(-\beta H^2 w^5 + \frac{K}{H} \right) \, dt = 0 .$$
(2.21)

Assuming

$$w << H_0$$

we can replace H by $H = H_0 + w \approx H_0$ in equation (2.20) to get

$$\frac{\partial w}{\partial t} = \frac{DH_0^3}{3\eta} w^{VI} - \frac{H_0^3 \alpha}{3\eta} \left(w^4 \right)'' + H_0^3 \beta \left(w^5 \right)' .$$
(2.22)

Structurally the model (2.22) is similar to the spinning combustion equation [19] and the model of non-local reaction-diffusion system [17, 18]. An individual pulse is formed by the dynamical balance between the three terms in the RHS of (2.22),

$$H_0^3 \frac{D}{3\eta} w^{VI} \sim -H_0^3 \frac{\alpha}{3\eta} \left(w^4 \right)'' \sim H_0^3 \beta \left(w^5 \right)' .$$
(2.23)

This relationship determines the characteristic scales for the height, Δw, and width, Δx, of an individual pulse. They will be independent of H_0 since H_0^3 can be cancelled out in (2.23) (for the adopted versions of the active stress and pressure; note that other versions are possible, in which case w may depend on H_0).

An extension of the model to cylindrical geometry is done using polar coordinates. In this case, instead of H_0 we use the neutral radius of the cylinder R_0 so that the displacement is introduced by

$$R(x, t) = R_0 + w .$$

We also need to modify the pressure equations (2.13)–(2.14) to include the term representing the Hooke's law. It expresses the passive effect of the increase of the radius if the pressure is increased. For the planar case analyzed above, the two planes are not directly connected to each other, therefore this term was absent. From the viewpoint of the resulting w-equation, it does not matter where we insert it, into (2.13) or (2.14), so let us insert into (2.14),

$$p_1 = -\alpha w^4 + \gamma w , \quad \alpha > 0 , \ \gamma > 0 .$$
(2.24)

Derivation process of the w-equation is similar to the planar case, and instead of $(-\alpha w^4)$ we use $(-\alpha w^4 + \gamma w)$. The final equation for cylindrical geometry is

$$\frac{\partial w}{\partial t} = \frac{DR_0^3}{16\eta} w^{VI} - \frac{R_0^3}{16\eta}\alpha \left(w^4\right)'' + \frac{R_0^3}{16\eta}\gamma w'' + \frac{R_0^3\beta}{2}\left(w^5\right)'. \tag{2.25}$$

Relative to the planar case, equation (2.25) also has the 2nd-order dissipative term $\sim w''$. It may affect the pulse characteristics, such as hight and speed, but will not change the pulse-generating dynamical balance (2.23).

3. Numerical approach

For solving equation (2.22) we developed numerical codes based on the one-dimensional integration radial basis function network (1D-IRBFN) method (Appendix A). Equation (2.22) is discretized with respect to both time and space variables. Firstly, the time interval $[0, T]$ is partitioned into N subintervals $[t^{(n)}, t^{(n+1)}]$ of length $\Delta t = T/N$ with $t^{(0)} = 1$ and $t^{(N+1)} = T$. The discretization of the problem in time is then accomplished by a time stepping scheme, followed by the spatial discretization based on the IRBFN method. Among many possible time-stepping schemes, the standard θ-scheme [13], $0 \le \theta \le 1$, is used in this work,

$$\frac{w^{(n+1)} - w^{(n)}}{\Delta t} = \theta W^{(n+1)} + (1-\theta)W^{(n)}, \tag{3.1}$$

where W denotes the RHS of (2.22). Note that the case $\theta = 0$ corresponds to the explicit forward Euler method and $\theta = 1$ to the implicit backward Euler method. The scheme associated with the case $\theta = 1/2$ is equivalent to the (semi-implicit) Crank–Nicolson method which is second-order accurate. Using $\theta = 1/2$ in (3.1) gives

$$\frac{w^{(n+1)} - w^{(n)}}{\Delta t} = \frac{1}{2}W^{(n+1)} + \frac{1}{2}W^{(n)}. \tag{3.2}$$

Denoting

$$A = \frac{DH_0^3}{3\eta}, \quad B = \frac{\alpha H_0^3}{3\eta}, \quad C = H_0^3\beta,$$

gives the discretized equation (3.2) in the form

$$\frac{w^{(n+1)} - w^{(n)}}{\Delta t} = \frac{1}{2}\left\{Aw^{VI} - B\left(w^4\right)'' + C\left(w^5\right)'\right\}^{(n+1)}$$

$$+ \frac{1}{2}\left\{Aw^{VI} - B\left(w^4\right)'' + C\left(w^5\right)'\right\}^{(n)}$$

or

$$\frac{w^{(n+1)}}{\Delta t} - \frac{1}{2}\left\{Aw^{VI} - B\left(w^4\right)'' + C\left(w^5\right)'\right\}^{(n+1)}$$

$$= \frac{w^{(n)}}{\Delta t} + \frac{1}{2}\left\{Aw^{VI} - B\left(w^4\right)'' + C\left(w^5\right)'\right\}^{(n)}, \tag{3.3}$$

where a dash is used again to denote the x-derivatives, $\triangle t = t^{(n+1)} - t^{(n)}$ is the time step. Equation (3.3) is then discretized in space based on the 1D-IRBFN method. After inserting appropriate values of w and its derivatives using (A.8), equation (3.3) is written as

$$E_1 \widehat{\alpha}^{(n+1)} = \text{RHS}_1 \tag{3.4}$$

and the boundary conditions as

$$E_2 \widehat{\alpha}^{(n+1)} = \text{RHS}_2 \,. \tag{3.5}$$

The system of equations (3.4)–(3.5) is solved simultaneously at each time step for $\widehat{\alpha}^{(n+1)}$ until the prescribed time T is reached.

4. Single-pulse regimes

In this section, we present basic numerical solutions of the non-dimensional form of equation (2.22),

$$\frac{\partial w}{\partial t} = Aw^{VI} - B\left(w^4\right)'' + C\left(w^5\right)' \,. \tag{4.1}$$

The non-dimensional coefficients A, B, and C are supposed to be a result of some non-dimensionalization procedure applied to equation (2.22). We now summarize the steps leading to (4.1): from (2.17) follows (2.20) upon neglecting the E-term; from (2.20) follows (2.22) by assuming $H = H_0 + w \approx H_0$; and finally from (2.22) follows (4.1) after non-dimensionalization.

By re-scaling t, x, and f, equation (4.1) can be set to a canonical form where the coefficients A, B, and C are made units. Therefore, regardless of the coefficient values used in a particular experiment, the shape of the function $w(x,t)$ simultaneously represents the shape of the solution of the canonical form of the equation only in re-scaled coordinates.

We started by selecting the coefficient values, domain size, and the initial condition. They need to provide a reasonable (not too long) time for the dynamic to reach a settled stage (when the pulse is formed) and guarantee sufficient spatial resolution of the main hump and also the oscillatory tail (resulting from the 6th-order dissipation) visible on every graph. The initial condition needs to be large enough in order to prevent collapse into a trivial state $w(x,t) =$const, corresponding to the absence of motion. Eventually, we chose $A = 1$, $B = 0.9$, and $C = 1$ and the size of the domain as shown by figures. The initial conditions are shown in the figures. The typical number of grid points was 100, the time step 0.001.

In the first series of experiments, the boundary conditions are chosen homogeneous, that is zero values of the function and its first two derivatives on the left and on the right edges,

$$w^{(k)}(x_0) = 0, \quad w^{(k)}(x_0 + L) = 0 \,, \quad k = 0, 1, 2 \,.$$

Figure 2 shows the snapshots of the settled regime – it has the form of the pulse propagating to the left. This is a typical outcome of the single-pulse experiments demonstrating the formation of the pulse from an arbitrarily set initial condition. The pulse can only continue in this form until the presence of the boundary is felt. Figure 3 shows how the pulse decays after hitting the boundary.

In the second series of numerical experiments, we used periodic boundary conditions with the period L,

$$w^{(k)}(x_0) = w^{(k)}(x_0 + L) \,, \quad k = 0, 1, 2, 3, 4, 5 \,.$$

Figure 4 shows snapshots of the solution at early times. After a while, the solution takes the familiar pulse form as shown in Figure 5.
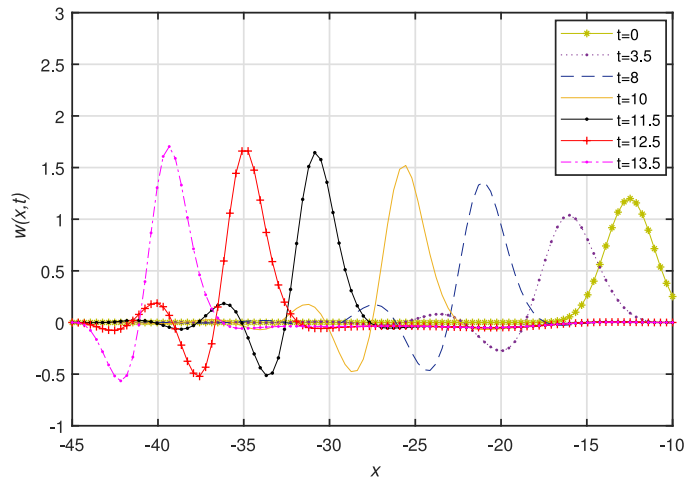
FIGURE 2. The initial condition $w(x, 0) = 1.2 \cdot \exp[-0.25(x + 12.5)^2]$. The snapshots are for the moments $t = 0, 3.5, 8, 10, 11.5, 12.5, 13.5$.
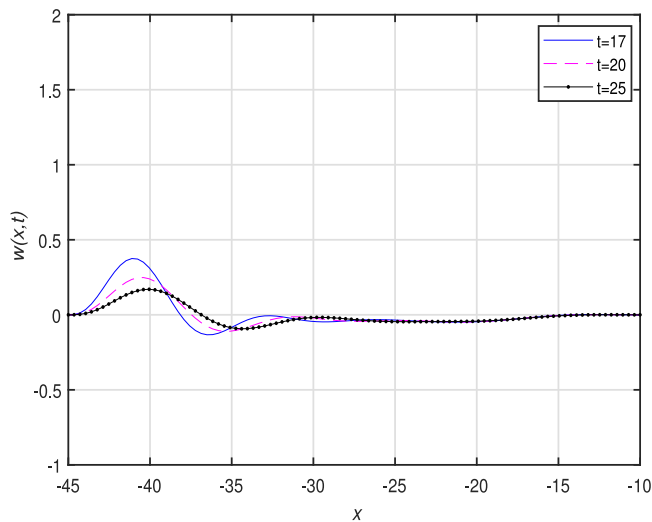

FIGURE 3. Continuation from Figure 2. $t = 17, 20, 25$.

5. MASS FLUX

Using the obtained periodic solution, let us calculate the mass flux through the cross-section of the channel. We note that integrating a travelling wave as a function of $\xi = x + \lambda t$ over one period in time, T, is equivalent to integrating over one period in space, so we will replace dt by dx/λ, where λ is the wave speed. Using (2.3), the instantaneous flux equals

$$Q = H \frac{\partial u}{\partial t} - \frac{H^3}{3\eta} p' \, .$$
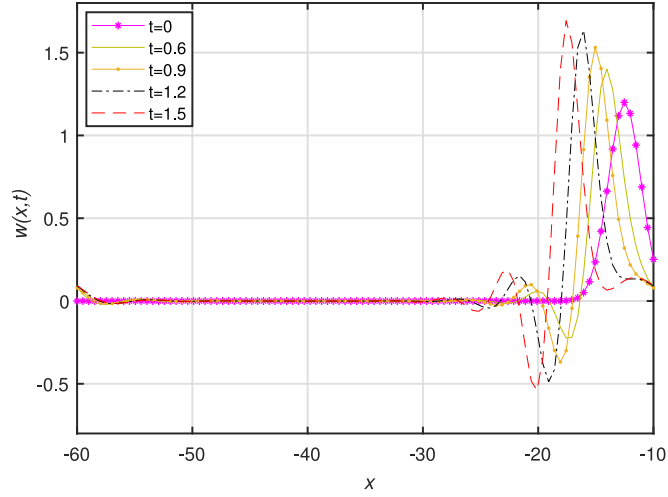
FIGURE 4. The initial condition $w(x,0) = 1.2 \exp[-0.25(x+12.5)^2]$. The snapshots are for $t = 0, 0.6, 0.9, 1.2, 1.5$.
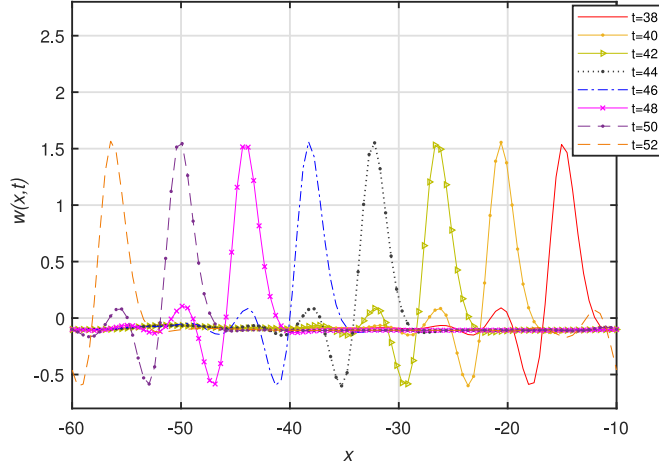
FIGURE 5. Continuation from Figure 4; $t = 38, 40, 42, 44, 46, 48, 50, 52$.

We substitute in here the expressions

$$p = Dw^{IV} - \alpha w^4$$

from (2.13) and (2.14) (recall that for the short model (2.22), the E-term in (2.13) disappears), and

$$H\frac{\partial u}{\partial t} = -\beta H^3 w^5 + K$$
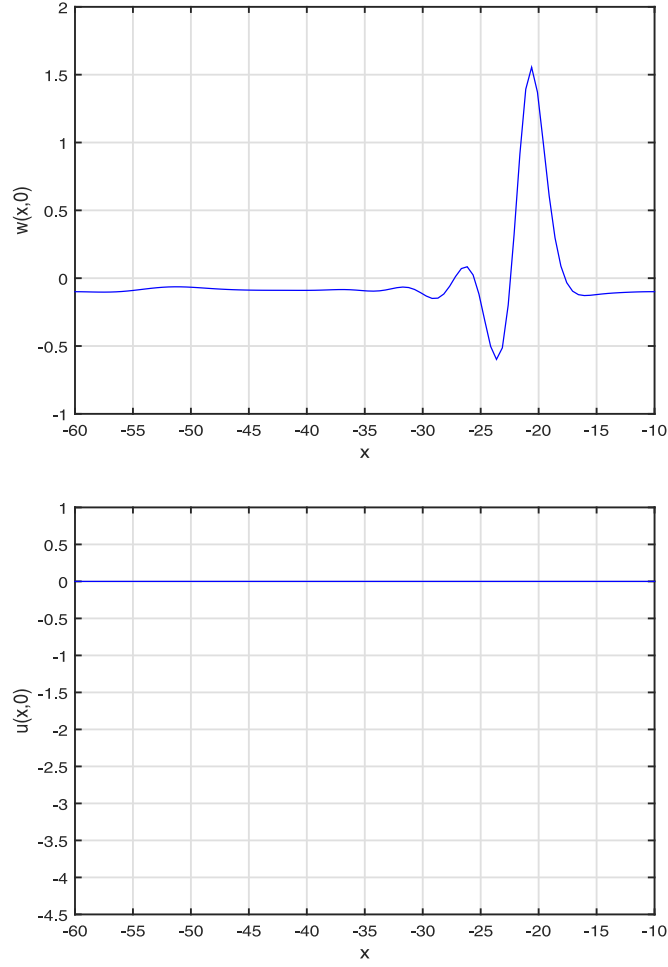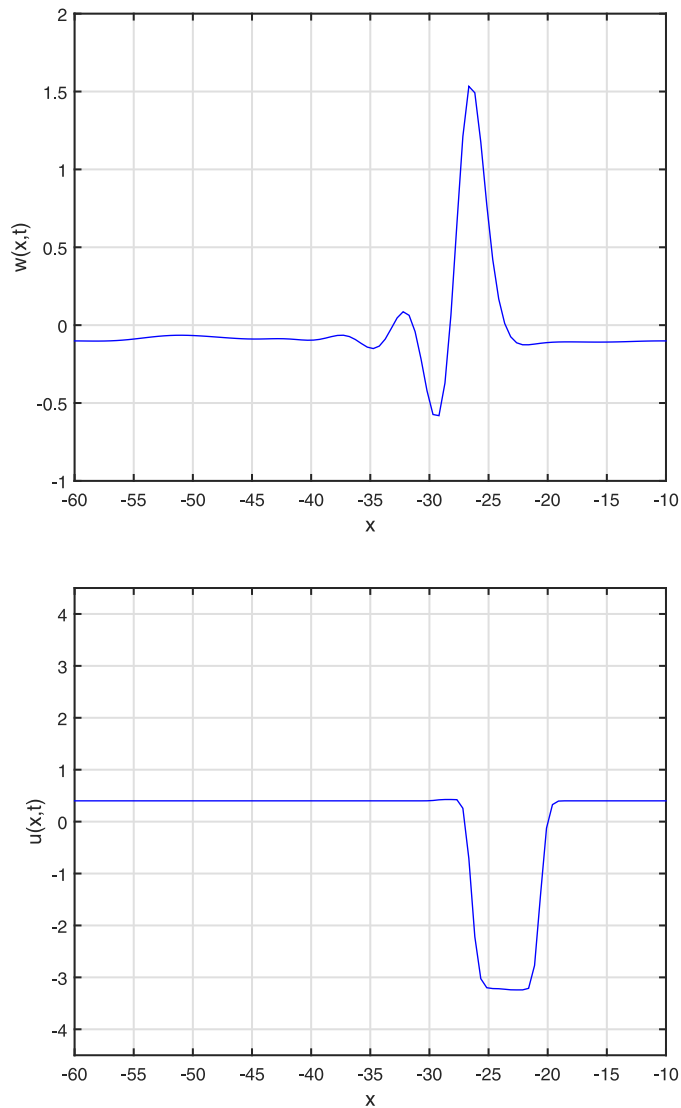
from (2.15), and

$$H = H_0 + w$$

FIGURE 6. The initial conditions for equation (5.2): the settled pulse for w and the zero displacement for u.

from (2.4). As a result, the total flux over one period

$$\int_T Q \, \mathrm{d}t = \frac{1}{\lambda} \int_L \left[-\beta (H_0 + w)^3 w^5 + K \right] \, \mathrm{d}x - \frac{1}{3\eta\lambda} \int_L (H_0 + w)^3 \left[Dw^V - \alpha \left(w^4 \right)' \right] \, \mathrm{d}x$$

$$\approx -\frac{H_0^3 \beta}{\lambda} \int_L \left(1 + 3\frac{w}{H_0} + \dots \right) w^5 \, \mathrm{d}x + \frac{KL}{\lambda}$$

$$- \frac{H_0^3}{3\eta\lambda} \int_L \left[1 + 3\frac{w}{H_0} + 3 \left(\frac{w}{H_0} \right)^2 + \dots \right] \left[Dw^V - \alpha \left(w^4 \right)' \right] \, \mathrm{d}x. \tag{5.1}$$

FIGURE 7. Continuation from Figure 6, $t = 2$.

Looking at the last integral in (5.1), we realize that, due to periodicity,

$$\int_L w^V \, \mathrm{d}x = 0 \,, \quad \int_L \left(w^4 \right)' \, \mathrm{d}x = 0 \,.$$

Furthermore, integrating by parts,

$$\int_L w \cdot w^V \, \mathrm{d}x = 0 \,, \qquad \int_L w \cdot \left(w^4 \right)' \, \mathrm{d}x = 0 \,.$$

Consequently, the input from the last integral in (5.1), representing the input from the pressure gradient, is quadratic in small "parameter" w/H_0. Let us show that the input from the shear stress is linear in w/H_0 and,
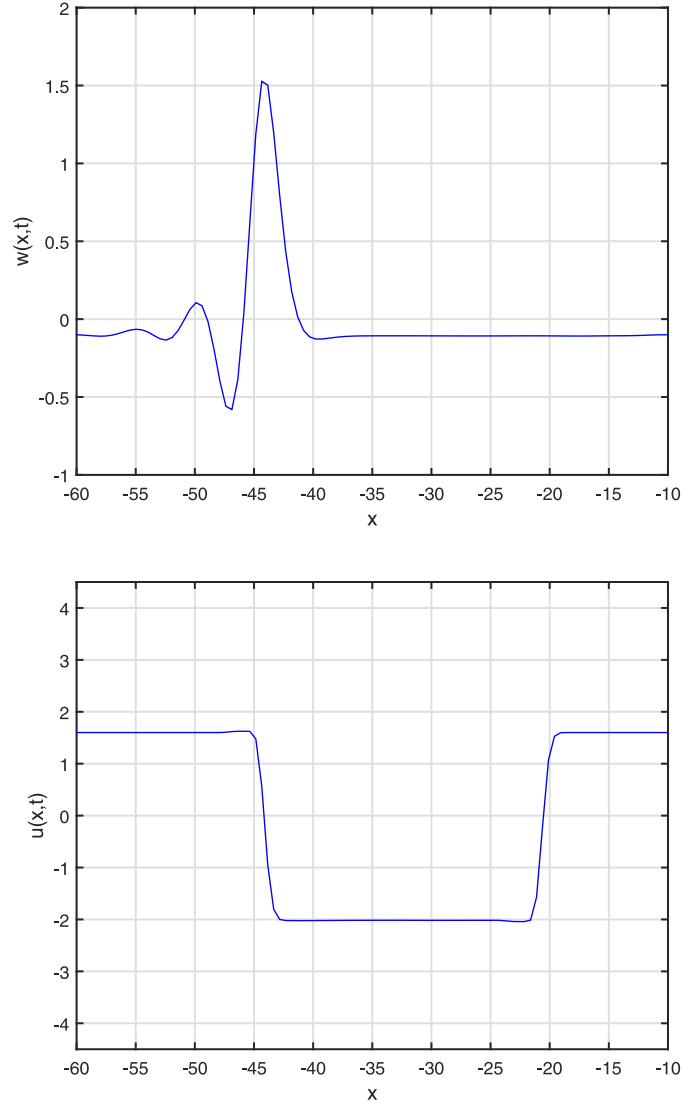
FIGURE 8. Continuation from Figure 7, $t = 8$.

therefore, makes major contribution into the flux. First, we need to determine K from the condition of zero displacement of the wall after one period. We are going to integrate $\partial u / \partial t$ and require that the total change of u over one period be zero. While u is measured in cm, it does not represent a displacement of any particular physical particle, but measures the amount of different particles that pass by the location x during one period. Zero total change of u means that all the particles of the wall that moved from the left to the right should come back from the right to the left by the end of one period. This process is illustrated below in Figures 6–11. Using (2.21) we have
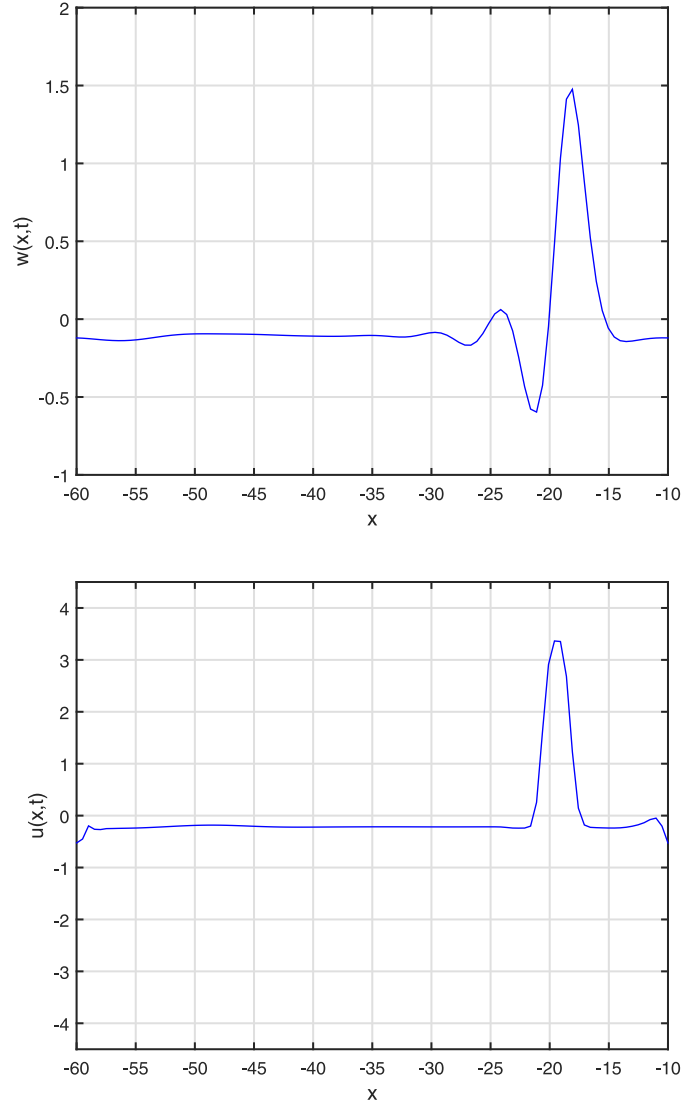
$$
\begin{aligned}
0 \quad &= \int_T \frac{\partial u}{\partial t} \, \mathrm{d}t = \frac{1}{\lambda} \int_L \left[-(H_0 + w)^2 \beta w^5 + \frac{K}{H_0 + w} \right] \, \mathrm{d}x \\
&\approx \frac{1}{\lambda} \int_L \left[-H_0^2 \left(1 + 2\frac{w}{H_0} + \dots \right) \beta w^5 + \frac{K}{H_0} \left(1 - \frac{w}{H_0} + \dots \right) \right] \, \mathrm{d}x \, .
\end{aligned}
$$
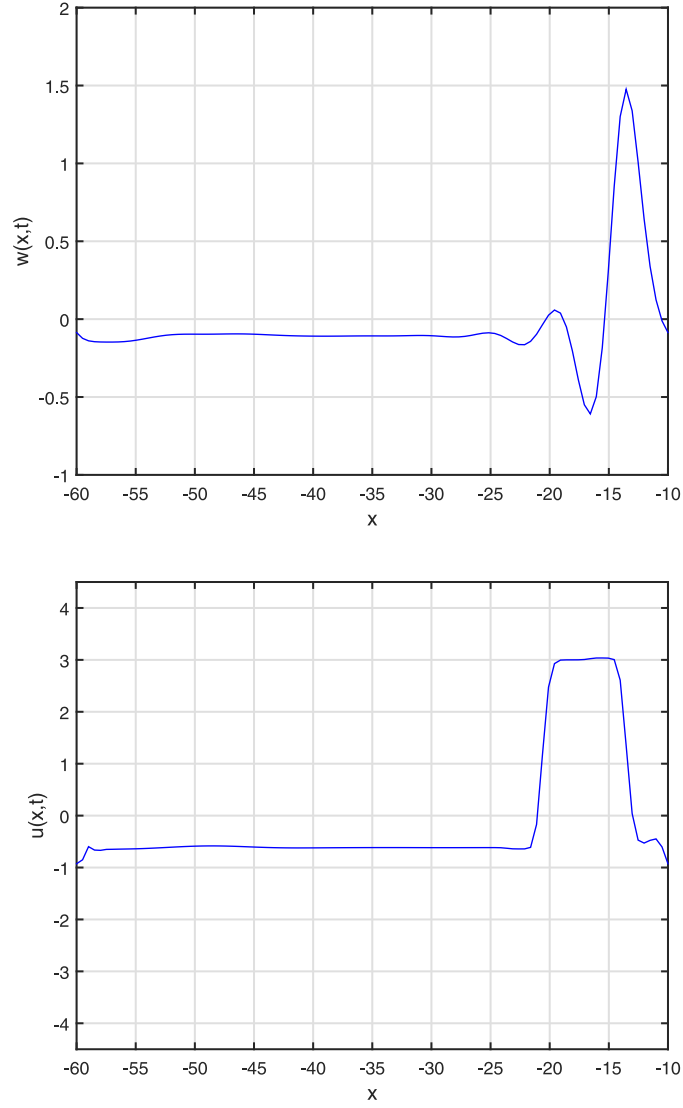
FIGURE 9. Continuation from Figure 8, $t = 15$.

Up to the linear terms in w/H_0,

$$K = \frac{H_0^3 \beta \left[\int_L w^5 \, \mathrm{d}x + 2 \int_L \left(\frac{w}{H_0} \right) w^5 \, \mathrm{d}x + \dots \right]}{L \left[1 - \frac{1}{L} \int_L \left(\frac{w}{H_0} \right) \, \mathrm{d}x + \dots \right]}$$

$$= \frac{H_0^3 \beta}{L} \left[\int_L w^5 \, \mathrm{d}x + 2 \int_L \left(\frac{w}{H_0} \right) w^5 \, \mathrm{d}x + \dots \right] \left[1 + \frac{1}{L} \int_L \left(\frac{w}{H_0} \right) \, \mathrm{d}x + \dots \right]$$
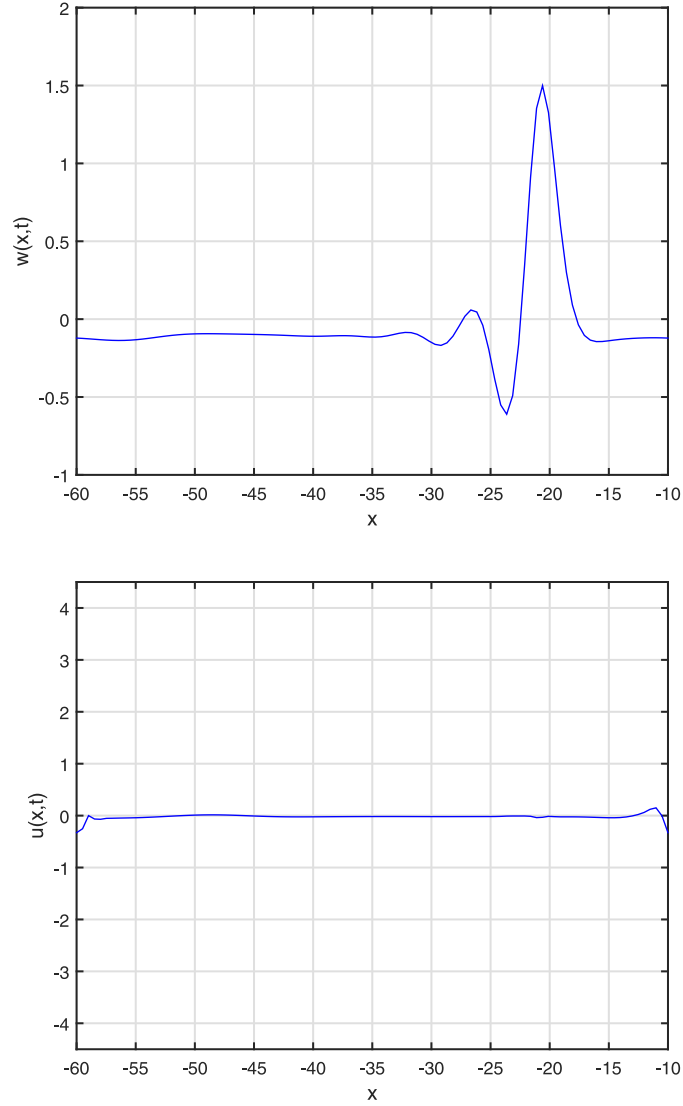
FIGURE 10. Continuation from Figure 9, $t = 17$.

$$\approx \frac{H_0^3 \beta}{L} \int_L w^5 \, \mathrm{d}x + \frac{2H_0^3 \beta}{L} \int_L \left(\frac{w}{H_0} \right) w^5 \, \mathrm{d}x + \frac{H_0^3 \beta}{L^2} \left(\int_L w^5 \, \mathrm{d}x \right) \cdot \left(\int_L \frac{w}{H_0} \, \mathrm{d}x \right) .$$

As a result,

$$\int_T Q \, \mathrm{d}t \approx -\frac{H_0^2 \beta}{\lambda} \int_L w^6 \, \mathrm{d}x + \frac{H_0^2 \beta}{\lambda L} \left(\int_L w^5 \, \mathrm{d}x \right) \cdot \left(\int_L w \, \mathrm{d}x \right) .$$

The dynamics of the horizontal displacement u according to the equation

$$\frac{\partial u}{\partial t} = -H_0^3 \beta w^5 + K \tag{5.2}$$

FIGURE 11. Continuation from Figure 10, $t = 18$.

is shown in Figures 6–11. Observe that at each location x the wall quickly moves to the left with the pulse during its immediate passage and then slowly returns to its original position. For the shown experiment, taking into account that $L = 50$, we compute

$$\int_L w^6 \, dx = 12.4 \,, \quad \int_L w^5 \, dx = 8.9 \,, \quad \int_L w \, dx = -2.0 \,,$$

giving

$$\frac{\lambda}{H_0^2 \beta} \int_L Q \, dt = -\int_L w^6 \, dx + \frac{1}{L} \left(\int_L w^5 \, dx \right) \left(\int_L w \, dx \right) = -12.7 \,. \tag{5.3}$$
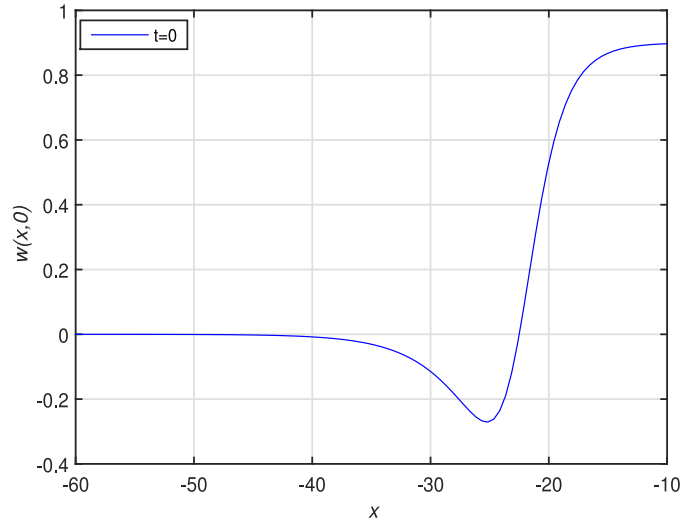
FIGURE 12. The initial condition $w(x,0) = 0.9 \left[\exp(0.23(x+22.5)) - \exp(-0.23(x+22.5))\right]$ $/ \left[\exp(0.23(x+22.5)) + \exp(-0.5(x+22.5))\right]$.
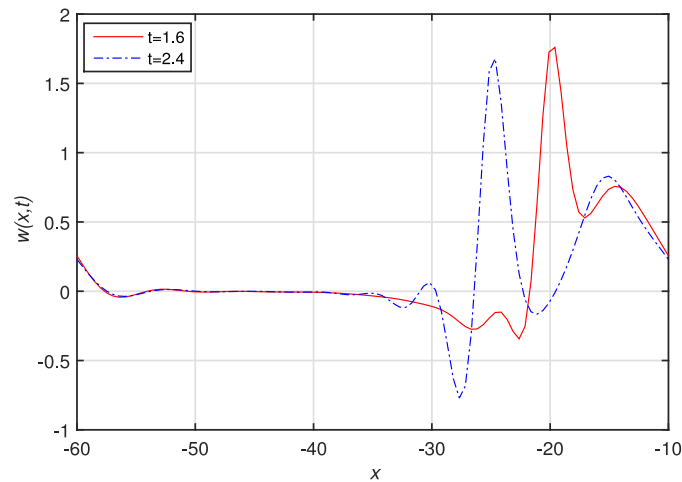

FIGURE 13. The snapshots at $t = 1.6, 2.4$.

An important thing is that the flux is non-zero and negative. In support of this result, in Appendix B we present an evaluation of the flux based on a simplified step-like sketch of the pulse.

6. MULTIPLE-PULSE REGIMES

In the next numerical experiment, the initial condition was chosen in the form of a large hump displayed in Figure 12. Obviously this shape is not consistent with the periodic boundary conditions, however, the equation quickly enforces periodicity (Fig. 13).

See that after some time the big hump breaks down into two pulses. We ran these experiments until the motion settled as demonstrated in Figure 14. It shows the settled two-pulse formation separated by roughly one cycle; this is why we see four pulses. A single snapshot in Figure 15 reveals that there are actually only two pulses at a moment.
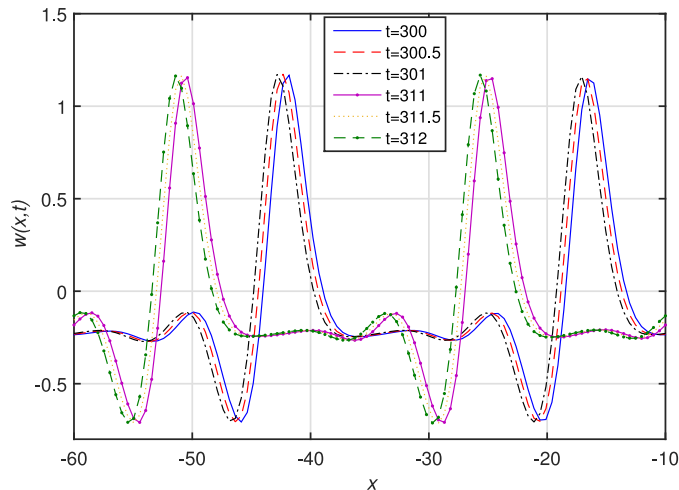
FIGURE 14. Continuation from Figure 13, the settled stage of the evolution. The snapshots are for the three close moments $t = 300, 300.5, 301$ and another three close moments $t = 311, 311.5, 312$.
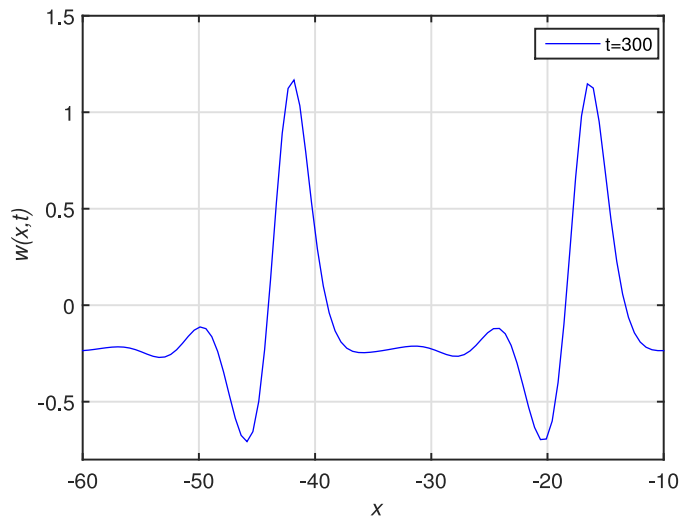

FIGURE 15. A selected profile from Figure 14, $t = 300$.

We observe from Figures 13–15 that the pulses gradually move away from each other before settling certain distance apart. Generally, for any experiment where two pulses are formed within one period L, the question is which of the following possibilities eventually realizes. Possibility 1: the distance between the pulses increases until the leading pulse (call it pulse 1) catches up with pulse 2 from behind, after which they merge back into a single pulse. In this case the distance, if measured from pulse 2 to pulse 1 from right to left, would become one full period. Possibility 2: the distance between the pulses becomes half the period. In this regime, the pulses may move either (a) without oscillations, or (b) with oscillations. Possibility 3: after an initial period of increase, the distance between the pulses decreases back to zero and the pulses re-combine. Possibility 4: the distance goes to (or oscillates about) a constant level which is not equal to half the period. In this and other similar experiments that we ran, possibility 2(b) realized, with the oscillations being relatively small. This is illustrated by Figure 16.
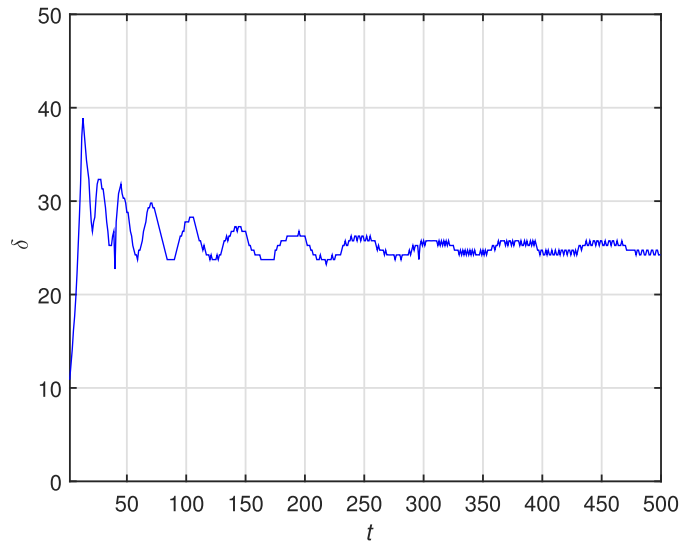
FIGURE 16. The evolution of the distance between two pulses. The period $L = 50$.
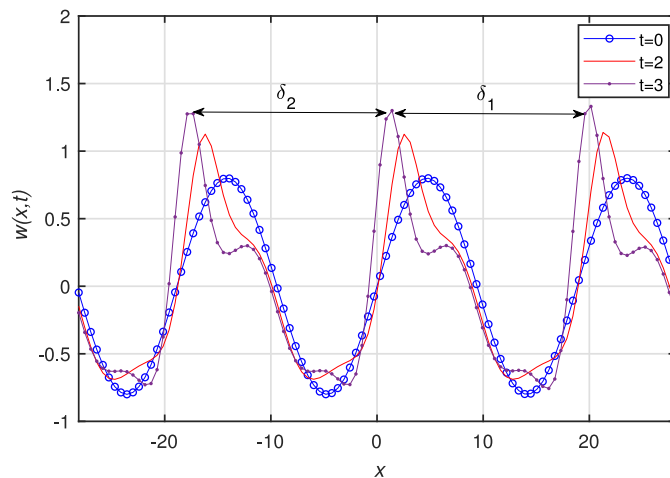

FIGURE 17. Formation of a three-pulse regime from the initial condition $w(x,0) = 0.8\sin(x/3)$. The snapshots are for $t = 0, 2, 3$.

Our next group of experiments deal with three-pulse regimes within one period L. Of course, three pulses can be created in many different ways, and we chose to seed them by an initial condition shaped as three sinusoidal crests, see Figure 17. This figure also shows an early stage of the evolution. After a sufficiently long time the solution settles in the form shown in Figure 18. We measured the distance δ_1 between the leading pulse 1 and the following pulse 2 and the distance δ_2 between the latter and the following pulse 3. Eventually an oscillatory regime settles as shown in Figure 19. The average values about which the oscillations occur are $\delta_1 = 17$ and $\delta_2 = 19$. Taking into account the period $L = 56.2$, the pulse 3–pulse 1 separation equals $\delta_3 = 56.2 - 17 - 19 = 20.2$. Thus, the separation of the pulses over the length of the period is not uniform unlike in the previous case of two pulses.

In general, this is an expected dynamic as multiple-pulse formations inevitably incur interaction of pulses via their tails. The more pulses are seeded within one period L and the larger the period, the more non-uniform
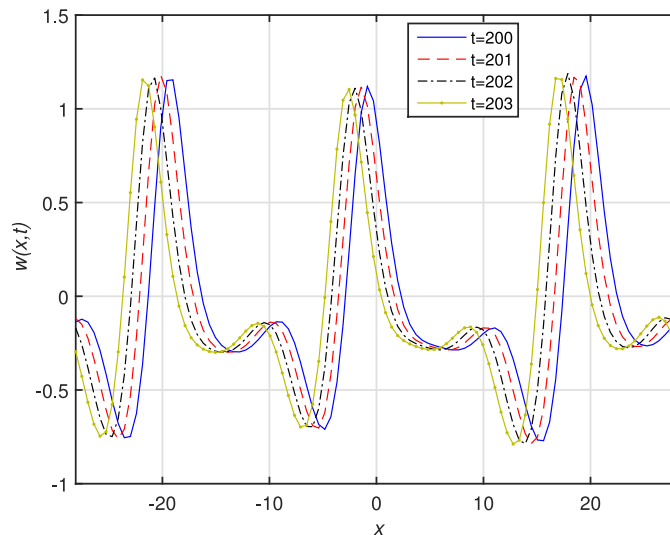
FIGURE 18. Continuation from Figure 17, $t = 200, 201, 202, 203$.
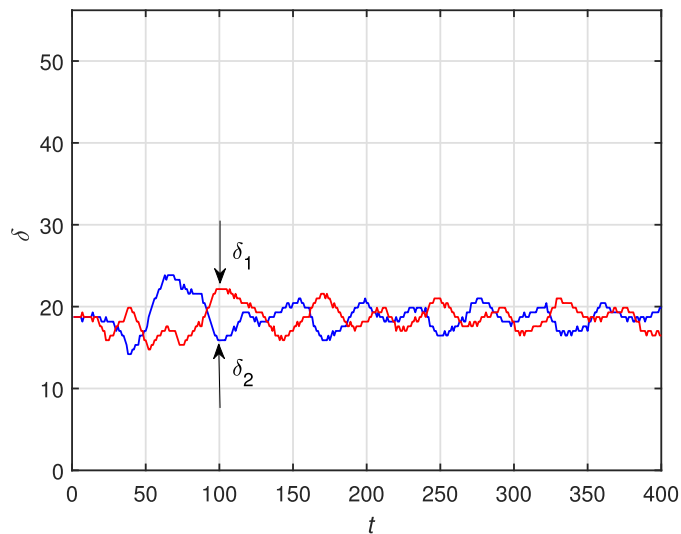
FIGURE 19. The evolution of the distance between three pulses. The period $L = 56.2$.

dynamics may be expected. However, one should bear in mind that any artificial or real artery has limited length; it is bounded by branching points where special boundary conditions need to replace our conditions of periodicity. We leave this issue outside of the scope of this paper.

7. Conclusion

We presented numerical solutions of the model describing auto-pulses in a channel simulating an artificial artery with active elastic walls. Viscosity plays dominant role over inertia in the model. For simplicity we adopted an unbounded plain channel geometry and smallness of the wall deflection. We demonstrated the process of formation of a pulse from an arbitrary initial condition. The fluid mass flux carried out by the pulse is calculated. Subject to spatially periodic boundary conditions, the system generates regimes with one, two, or

more pulses within one spatial period. We investigated the time-dependence of the distance between adjacent pulses in a two-pulse regime and detected small sustained fluctuations. Three-pulse regimes are also explored. The numerical experiments show slight non-uniformity of the average pulse separation and the presence of relatively small fluctuations.

Appendix A

The 1D-IRBFN method has been successfully used for solving a variety of problems such as fluid structure interaction [12], viscous and viscoelastic flows [5, 21], and structural analysis [11]. The 1D-IRBFN method is an improved version of the original IRBFN method presented in [10]. In this method highest-order derivative in a differential equation is approximated by radial basis functions and, further, the lower-order derivatives and function itself are then obtained by integration. The purpose of using integration is to avoid the reduction in convergence rate caused by differentiation and also to improve the numerical stability of a discrete solution. In the present paper, we use the following notations: $\widehat{[\,]}$ for a vector/matrix $[\,]$ that is associated with a grid line, and $[\,]_{(n)}$ to denote selected components of the vector $[\,]$. There are many types of radial basis functions (RBFs) such as Gaussians, multiquadrics (MQ), inverse multiquadrics, and thin plate spline. Owing to the excellent performance of the multiquadric RBFs in the function approximation [3], we use it in this work. The MQ-RBFs have the following form,

$$G_i(x) = \sqrt{\left(x - c_i\right)^2 + a_i{}^2}\,,$$

where c_i and a_i are the centre and width of the i-th MQ-RBF, respectively. The set of centres is chosen to be the same as the set of collocation points, and the RBF width is determined as $a_i = bd_i$, $b > 0$ is a factor (presently $b = 1$), and d_i is the distance from the i-th centre to the nearest. The domain of interest is discretized using a uniform Cartesian grid having N nodes on the x-axis.

Applying the basic idea of the integral RBF form [10] we decompose a 6th-order derivative of the function w into RBFs. The RBF networks are then integrated to obtain the lower-order derivatives and the function itself. We have

$$\frac{\partial^6 w(x,t)}{\partial x^6} = \sum_{i=1}^{N} u_i(t) G_i(x) = \sum_{i=1}^{N} u_i(t) H_6^{(i)}(x)\,, \tag{A.1}$$

$$\frac{\partial^5 w(x,t)}{\partial x^5} = \sum_{i=1}^{N} u_i(t) H_5^{(i)}(x) + c_1\,, \tag{A.2}$$

$$\frac{\partial^4 w(x,t)}{\partial x^4} = \sum_{i=1}^{N} u_i(t) H_4^{(i)}(x) + c_1 x + c_2\,, \tag{A.3}$$

$$\frac{\partial^3 w(x,t)}{\partial x^3} = \sum_{i=1}^{N} u_i(t) H_3^{(i)}(x) + \frac{c_1}{2} x^2 + c_2 x + c_3\,, \tag{A.4}$$

$$\frac{\partial^2 w(x,t)}{\partial x^2} = \sum_{i=1}^{N} u_i(t) H_2^{(i)}(x) + \frac{c_1}{6} x^3 + \frac{c_2}{2} x^2 + c_3 x + c_4\,, \tag{A.5}$$

$$\frac{\partial w(x,t)}{\partial x} = \sum_{i=1}^{N} u_{(i)}(t) H_1^{(i)}(x) + \frac{c_1}{24} x^4 + \frac{c_2}{6} x^3 + \frac{c_3}{2} x^2 + c_4 x + c_5\,, \tag{A.6}$$

$$w(x,t) = \sum_{i=1}^{N} u_{(i)}(t) H_0^{(i)}(x) + \frac{c_1}{120} x^5 + \frac{c_2}{24} x^4 + \frac{c_3}{6} x^3 + \frac{c_4}{2} x^2 + c_5 x + c_6\,, \tag{A.7}$$

where $\{G_i(x)\}_{i=1}^{N} = \{H_6^{(i)}(x)\}_{i=1}^{N}$ are known RBFs; $H_5^{(i)}(x) = \int H_6^{(i)}(x)dx$; $H_4^{(i)}(x) = \int H_5^{(i)}(x)dx$; $H_3^{(i)}(x) = \int H_4^{(i)}(x)dx$; $H_2^{(i)}(x) = \int H_3^{(i)}(x)dx$; $H_1^{(i)}(x) = \int H_2^{(i)}(x)dx$; $H_0^{(i)}(x) = \int H_1^{(i)}(x)dx$; $\{c_i\}_{i=1}^{6}$ the set of constants arising from integration. The new basis functions $H_5^{(i)}(x)$, $H_4^{(i)}(x)$, $H_3^{(i)}(x)$, $H_2^{(i)}(x)$, and $H_1^{(i)}(x)$ are obtained from integrating the multiquadrics as follows,

$$H_5^{(i)}(x) = \frac{r}{2}\sqrt{r^2 + a_i^2} + \frac{a_i^2}{2}\ln\left|r + \sqrt{r^2 + a_i^2}\right|,$$

$$H_4^{(i)}(x) = \left(\frac{r^2}{6} - \frac{a_i^2}{3}\right)\sqrt{r^2 + a_i^2} + \frac{a_i^2 r}{2}\ln\left|r + \sqrt{r^2 + a_i^2}\right|,$$

$$H_3^{(i)}(x) = \left(\frac{r^3}{24} - \frac{13a_i^2 r}{48}\right)\sqrt{r^2 + a_i^2} + \left(\frac{a_i^2 r^2}{4} - \frac{a_i^4}{16}\right)\ln\left|r + \sqrt{r^2 + a_i^2}\right|,$$

$$H_2^{(i)}(x) = \left(\frac{r^4}{120} - \frac{83a_i^2 r^2}{720} + \frac{a_i^4}{45}\right)\sqrt{r^2 + a_i^2} + \left(\frac{a_i^2 r^3}{12} - \frac{a_i^4 r}{16}\right)\ln\left|r + \sqrt{r^2 + a_i^2}\right|\Big),$$

$$H_1^{(i)}(x) = \left(\frac{r^5}{720} - \frac{97a_i^2 r^3}{2880} + \frac{113a_i^4 r}{5760}\right)\sqrt{r^2 + a_i^2}$$
$$+ \left(\frac{a_i^2 r^4}{48} - \frac{a_i^4 r^2}{32} + \frac{a_i^6}{384}\right)\ln\left|r + \sqrt{r^2 + a_i^2}\right|,$$

$$H_0^{(i)}(x) = \left(\frac{r^6}{5040} - \frac{253a_i^2 r^4}{33600} + \frac{593a_i^4 r^2}{67200} - \frac{a_i^6}{1575}\right)\sqrt{r^2 + a_i^2}$$
$$+ \left(\frac{a_i^2 r^5}{240} + \frac{a_i^6 r}{384} - \frac{a_i^4 r^3}{96}\right)\ln\left|r + \sqrt{r^2 + a_i^2}\right|,$$

where $r = x - c_i$. After discretization, equations (A.1)–(A.7) can be written in a compact form as

$$\widehat{\frac{\partial^6 w}{\partial x^6}} = \widehat{H_6^{(i)}}\widehat{\alpha}, \quad \widehat{\frac{\partial^5 w}{\partial x^5}} = \widehat{H_5^{(i)}}\widehat{\alpha}, \quad \widehat{\frac{\partial^4 w}{\partial x^4}} = \widehat{H_4^{(i)}}\widehat{\alpha},$$

$$\widehat{\frac{\partial^3 w}{\partial x^3}} = \widehat{H_3^{(i)}}\widehat{\alpha}, \quad \widehat{\frac{\partial^2 w}{\partial x^2}} = \widehat{H_2^{(i)}}\widehat{\alpha}, \quad \widehat{\frac{\partial w}{\partial x}} = \widehat{H_1^{(i)}}\widehat{\alpha}, \quad \widehat{w} = \widehat{H_0^{(i)}}\widehat{\alpha}, \tag{A.8}$$

where

$$\widehat{H_6^{(i)}} = \begin{bmatrix} H_6^{(1)}(x_1) & H_6^{(2)}(x_1) & \dots & H_6^{(N)}(x_1) & 0 & 0 & 0 & 0 & 0 & 0 \\ H_6^{(1)}(x_2) & H_6^{(2)}(x_2) & \dots & H_6^{(N)}(x_2) & 0 & 0 & 0 & 0 & 0 & 0 \\ \dots & \dots & \dots & \dots & \dots & \dots & \dots & \dots & \dots & \dots \\ H_6^{(1)}(x_N) & H_6^{(2)}(x_N) & \dots & H_6^{(N)}(x_N) & 0 & 0 & 0 & 0 & 0 & 0 \end{bmatrix}, \tag{A.9}$$

$$\widehat{H_5^{(i)}} = \begin{bmatrix} H_5^{(1)}(x_1) & H_5^{(2)}(x_1) & \dots & H_5^{(N)}(x_1) & 1 & 0 & 0 & 0 & 0 & 0 \\ H_5^{(1)}(x_2) & H_5^{(2)}(x_2) & \dots & H_5^{(N)}(x_2) & 1 & 0 & 0 & 0 & 0 & 0 \\ \dots & \dots & \dots & \dots & \dots & \dots & \dots & \dots & \dots & \dots \\ H_5^{(1)}(x_N) & H_5^{(2)}(x_N) & \dots & H_5^{(N)}(x_N) & 1 & 0 & 0 & 0 & 0 & 0 \end{bmatrix}, \tag{A.10}$$

$\ldots,$

$$\widehat{H_0^{(i)}} = \begin{bmatrix} H_0^{(1)}(x_1) & H_0^{(2)}(x_1) & \ldots & H_0^{(N)}(x_1) & x_1^5/5! & x_1^4/4! & x_1^3/3! & x_1^2/2! & x_1 & 1 \\ H_0^{(1)}(x_2) & H_0^{(2)}(x_2) & \ldots & H_0^{(N)}(x_2) & x_2^5/5! & x_2^4/4! & x_2^3/3! & x_2^2/2! & x_2 & 1 \\ \ldots & \ldots & \ldots & \ldots & \ldots & \ldots & \ldots & \ldots & \ldots & \ldots \\ H_0^{(1)}(x_N) & H_0^{(2)}(x_N) & \ldots & H_0^{(N)}(x_N) & x_N^5/5! & x_N^4/4! & x_N^3/3! & x_N^2/2! & x_N & 1 \end{bmatrix}, \tag{A.11}$$

where $\{x_i\}_{i=1}^N$ is the set of inputs, $\widehat{w} = (w_1, w_2, w_3, ..., w_N)^T$, $w_i = w(x_i, t)$, $\widehat{u} = (u_1, u_2, u_3, ..., u_N)^T$ and $\widehat{c} = (c_1, c_2, c_3, c_4, c_5, c_6)^T$. We denote $\widehat{\alpha} = (u_1, u_2, u_3, ..., u_N, c_1, c_2, ..., c_6)^T$.

Appendix B

We apply formula (5.3) to an approximate step-like configuration of the pulse as shown in Figure B.1. We have

$$\frac{\lambda}{H_0^2 \beta} \int_L Q \, \mathrm{d}t = -\int_L w^6 \, \mathrm{d}x + \frac{1}{L} \left(\int_L w^5 \, \mathrm{d}x \right) \cdot \left(\int_L w \, \mathrm{d}x \right)$$

$$= -w_0^6 \delta - w_1^6 (L - \delta) + \frac{1}{L} \left[w_0^5 \delta - w_1^5 (L - \delta) \right] \cdot \left[w_0 \delta - w_1 (L - \delta) \right]$$

$$= \frac{\delta(L - \delta)}{L} \left[-w_0^6 - w_1^6 - w_0^5 w_1 - w_0 w_1^5 \right] < 0$$

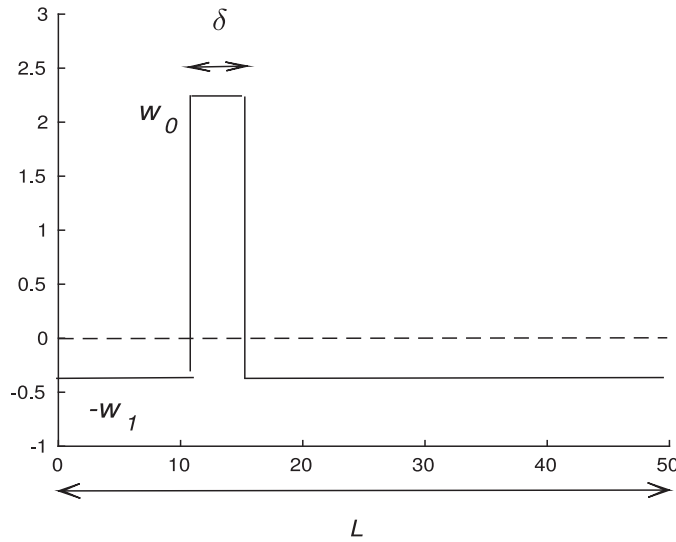for any $w_0 > 0$, $w_1 > 0$, and $L > \delta$.

FIGURE B.1. A primitive configuration of the pulse.

References

[1] F.Z. Ahmed, D.V. Strunin, M.G. Mohammed and R.P. Bhanot, Numerical solution for the fluid flow between active elastic walls. *ANZIAM J. (E)* **57** (2016) C221–C234.

[2] N. Bessonov, A. Sequeira, S. Simakov, Yu. Vassilevskii and V. Volpert, Methods of blood flow modelling. *MMNP* **11** (2016) 1–25.

[3] R. Franke, Scattered data interpolation: tests of some methods. *Math. Comput.* **38** (1982) 181–200.

[4] G.G. Haff and N.T. Triplett, Essentials of Strength Training and Conditioning, 4th edition. Human Kinetics, (2016).

[5] D. Ho-Minh, N. Mai-Duy and T. Tran-Cong, Simulation of viscous and viscoelastic flows using a RBF-Galerkin approach. *Aust. J. Mech. Eng.* **9** (2012) 101–112.

[6] R. Huang and Z. Suo, Wrinkling of a compressed elastic film on a viscous layer. *J. Appl. Phys.* **91** (2002) 1135–1142.

[7] C. Kleinstreuer, Biofluid Dynamics. Taylor and Francis, Boca Raton (2006).

[8] L.D. Landau and E.M. Lifshitz, Theory of Elasticity. Pergamon, London (1959) 57–60.

[9] S. Li, D.M. Vogt, D. Rus and R.J. Wood, Fluid-driven origami-inspired artificial muscles. In Vol. 114 of *Proc. of Nat. Acad. Sci. USA* (2017) 13132–13137.

[10] N. Mai-Duy and T. Tran-Cong, Numerical solution of differential equations using multiquadric radial basis function networks. *Neural Netw.* **14** (2001) 185–199.

[11] D. Ngo-Cong, N. Mai-Duy, W. Karunasena and T. Tran-Cong, Free vibration analysis of laminated composite plates based on FSDT using one-dimensional IRBFN method. *Comput. Model. Eng. Sci.* **89** (2011) 1–13.

[12] D. Ngo-Cong, N. Mai-Duy, W. Karunasena and T. Tran-Cong, A numerical procedure based on 1D-IRBFN and local MLS-1D-IRBFN methods for fluid-structure interaction analysis. *Comput. Model. Eng. Sci.* **83** (2012) 459–498.

[13] A. Quarteroni and A. Valli, Numerical Approximation of Partial Differential Equations. Springer-Verlag, New York (1997).

[14] A.J. Roberts, A One-Dimensional Introduction to Continuum Mechanics. World Scientific, Singapore (1994).

[15] S.J. Sherwin, L. Formaggia, J. Peiro and V. Franke, Computational modelling of 1D blood flow with variable mechanical properties and its application to the simulation of wave propagation in the human arterial system. *Int. J. Numer. Meth. Fluids* **43** (2003) 673–700.

[16] D.V. Strunin, Fluid flow between active elastic plates. *ANZIAM J. Aust. Math. Soc., Ser. B* **50** (2008) C871–C883.

[17] D.V. Strunin and M.G. Mohammed, Range of validity and intermittent dynamics of the phase of oscillators with nonlinear self-excitation. *Commun. Nonlinear Sci. Numer. Simul.* **29** (2015) 128–147.

[18] D.V. Strunin, Phase equation with nonlinear excitation for nonlocally coupled oscillators. *Phys. D: Nonlin. Phenom.* **238** (2009) 1909–1916.

[19] D.V. Strunin, Autosoliton model of the spinning fronts of reaction. *IMA J. Appl. Math.* **63** (1999) 163–177.

[20] S. Timoshenko and S. Woinowsky-Krieger, Theory of Plates and Shells. McGraw-Hill, New York (1987).

[21] C.D. Tran, N. Mai-Duy, K. Le-Cao and T. Tran-Cong, A continuum-microscopic method based on IRBFs and control volume scheme for viscoelastic fluid flows. *Comput. Model. Eng. Sci.* **85** (2012) 499–519.